https://doi.org/10.5194/egusphere-2025-4490
Preprint. Discussion started: 24 September 2025


# High resolution quantification of $SO_2$ emissions over India based on TROPOMI observations

Yutao Chen[1,2], Ronald J. van der A[1], Jieying Ding[1], Henk Eskes[1], Felipe Cifuentes[1,3], and Pieternel F. Levelt[4,2,1]

[1]Royal Netherlands Meteorological Institute (KNMI), De Bilt, the Netherlands
[2]Department of Geoscience & Remote Sensing, Delft University of Technology (TUD), Delft, the Netherlands
[3]Meteorology and Air Quality Department, Wageningen University & Research (WUR), Wageningen, the Netherlands
[4]National Center for Atmospheric Research (NCAR), Boulder, Colorado, United States

**Correspondence:** Yutao Chen (yutao.chen@knmi.nl) and Jieying Ding (jieying.ding@knmi.nl)

**Abstract**

India is a country with high sulfur dioxide ($SO_2$) emissions mainly resulting from the large number of coal-fired thermal power plants. $SO_2$ column observations from the Sentinel-5P Tropospheric Monitoring Instrument (TROPOMI) satellite instrument, in combination with inverse modelling techniques can be used to derive observation-based $SO_2$ emission estimates. The flux-divergence emission estimation method is sensitive to point source emissions and is well-suited for estimating $SO_2$ emissions in India. However, the flux-divergence method combined with satellite observations spreads out the calculated emissions to grid cells in the neighborhood of the point source. This spreading effect weakens the signal of point sources at their exact location, making it harder to quantify the exact emissions. In this paper, we describe a deconvolution algorithm to reverse the spreading and sharpen the emission signals. Our deconvolution algorithm ensures mass conservation of the emissions. We apply the deconvolution algorithm on gridded $SO_2$ emissions at a high spatial resolution of 0.025° × 0.025° (2.5km × 2.5km) derived from TROPOMI observations with a typical mean footprint size of 6 km. After the deconvolution, the effective spatial resolution of emissions is enhanced to match the grid cell resolutions. The point source emissions significantly increase at their exact locations and emissions in the neighbor grid cells become lower. In our inventory, about 80% of coal-based power plants with a capacity above 100 MW are detected at the correct location, while the remaining 20% fall below the noise level. The detected power plants account for 99% of India's total coal-based power generation. We also identify 7 previously unreported $SO_2$ point sources, including coal-based thermal power plants, cement plants, copper industry, and crude oil facility. This deconvolution algorithm improves emission detection and can also be used for other pollutants emitted by point sources to enhance the accuracy of emission inventories.

## 1 Introduction

$SO_2$ is a reactive gas-phase pollutant in the atmosphere. It can react with hydroxyl radicals to form sulfuric acid ($H_2SO_4$). It can also dissolve in cloud droplets to form sulfate ($SO_4^{2-}$) after reacting with hydrogen peroxide and ozone (Steinfeld, 1998). Atmospheric $SO_2$ and particulate $SO_4^{2-}$ negatively affect human health and the ecosystem. Exposure to $SO_2$ increases the rate of respiratory illness (Orellano et al., 2021; Tomić-Spirić et al., 2021). And the sulfuric acid rain acidifies the soil and water ecosystem and also damages buildings (Singh and Agrawal, 2007; Bhargava and Bhargava, 2013). Moreover, $SO_4^{2-}$ particles promotes cloud formation by increasing cloud condensation nuclei, which affects regional and global climate system (Arnold, 2006; Feldman et al., 2012). Atmospheric $SO_2$ sources includes natural sources, such as volcanic eruptions and passive degassing (Eisinger and Burrows, 1998; Oppenheimer et al., 2011) as well as anthropogenic sources, such as coal-based powerplants, metal smelting and refining, and other coal-combustion activities (Klimont et al., 2013; Serbula et al., 2014;

https://doi.org/10.5194/egusphere-2025-4490
Preprint. Discussion started: 24 September 2025


Kuttippurath et al., 2022; Kang et al., 2019). In rapidly developing countries like India, the growth of anthropogenic $SO_2$ emissions is closely related to thermal power generation (Chakraborty et al., 2008; Nazari et al., 2010; Yadav and Prakash, 2014). Over the past two decades, India's thermal power capacity has been continuously increasing from $7.4 \times 10^4$ MW to $2.4 \times 10^5$ MW (Patel, 2024). Since 2016, India has emitted most anthropogenic $SO_2$ in the world (Li et al., 2017a; Li et al., 2017b) , mainly from power plants. Despite this, the country still faces power shortages (Chan and Delina, 2023). In 2022, there was an estimated gap of 8,657 MW between power generation and peak demand (Central Electricity Authority, 2023). The Global Energy Monitor recently reported a record high in new coal plant requests in India (GEM, 2025). $SO_2$ emissions are expected to keep rising, because India continues to rely heavily on coal to meet its increasing energy demands driven by population growth and economic development (Kuttippurath et al., 2022). The often used bottom-up $SO_2$ emission inventory Emissions Database for Global Atmospheric Research version 8 (EDGARv8), has been updated to 2022 (Crippa et al., 2024). Its method first estimate emissions at the subnational level and then allocates the emissions to known point sources, which cannot fully capture the emergence of new point sources and rapid changes in emissions. A high-resolution, up-to-date $SO_2$ emission inventory is crucial for tracking changes of $SO_2$ emissions and identifying new sources across the country.

Satellite instruments can monitor atmospheric $SO_2$ in the thermal infrared (IR) and ultraviolet (UV) band of spectrum (Krueger et al., 2000; Eisinger and Burrows, 1998; Krueger, 1983; Bovensmann et al., 1999; Callies et al., 2000; Levelt et al., 2006; Veefkind et al., 2012; Taylor et al., 2018; Tournigand et al., 2020; Theys et al., 2021), enabling the estimation of $SO_2$ emissions through top-down methods. Two main inversion approaches, inverse modeling and mass balance methods, are commonly used to calculate $SO_2$ emissions from satellite observations. Inverse modeling methods estimate emissions of short-live gases like $SO_2$ by applying a correction to the bottom-up emissions, so that the simulated results align well with observations (Brasseur and Jacob, 2017). These methods depend on prior information to constrain and optimize the estimated emissions, and they are affected by uncertainties in transport models (Brasseur and Jacob, 2017; Qu et al., 2019; Wang et al., 2020). The dependency on prior information limits the ability of inverse modeling to detect new or unknown sources. In contrast, mass-balance methods, such as the plume fitting and flux-divergence methods, require less prior information, mainly using satellite $SO_2$ measurements and wind field data. In the plume fitting method, the total $SO_2$ amount near an individual source is derived from the fitting plume function of $SO_2$ measured density. Emissions are then calculated by integrating the $SO_2$ amount and adding the estimated sink term, which is based on a constant decay rate derived from the plume function (Fioletov et al., 2011; Fioletov et al., 2013; Fioletov et al., 2015; Fioletov et al., 2016). However, using a fixed decay rate can affect the accuracy of the sink estimation, especially for gases like $SO_2$ that have variable lifetimes (Krol et al., 2024; Chen et al., 2025). And the emissions calculated from the plume fitting method are not mapped on a regular grid. The flux-divergence method calculates emissions by adding the divergence and sink terms (Beirle et al., 2019). It has been used to estimate emissions of $NO_x$ (Beirle et al., 2021; Cifuentes et al., 2025), $CH_4$ (Liu et al., 2021), $CO_2$ (Hakkarainen et al., 2022), and $SO_2$ (Chen et al., 2025). Compared to inverse modeling, this method is more time and computational efficient, especially for generating emissions over large areas. Compared to the plume fitting method, the divergence method can generate gridded emissions. In theory, the divergence method works well for detecting and quantifying point source emissions. This is because steep concentration gradients at point sources produce clear divergence and emission signals (Beirle et al., 2019). In practical implementations, the calculation of the gridded divergence, which involves concentration differences between neighboring grid cells, will cause the emissions to spread, since the discretization of gridded concentrations during the calculation causes the divergence to be distributed not only at the point source locations but also over the surrounding grid cells (Chen et al., 2025). Additionally, the finite resolution of the satellite measurements will limit the capability to distinguish nearby point sources. Since satellite measurements are used in divergence calculations, their spatial resolution largely determines the finest possible resolution for the resulting gridded divergence terms. Reducing this spreading can improve both the accuracy and resolution of the emission inventory calculated using the divergence method.

https://doi.org/10.5194/egusphere-2025-4490
Preprint. Discussion started: 24 September 2025


In this study, we combine the divergence method and a deconvolution algorithm to update the gridded Indian $SO_2$ emission inventory into an effective high spatial resolution of 0.025° × 0.025° (approximately 2.5 km × 2.5 km) using daily $SO_2$ observations from the Tropospheric Monitoring Instrument (TROPOMI) instrument (Veefkind et al., 2012; Theys et al., 2017). We use the same method as Chen et al. (2025) to estimate Indian $SO_2$ emissions, calculated from the sum of the $SO_2$ divergence and sink term. Since our grid resolution is finer than the TROPOMI pixel size, the point source emissions tend to be spread out over multiple grid cells in the resulting inventory. In this paper we describe a deconvolution algorithm to remove this spreading, allowing the emissions to better reflect the true locations and strengths of sources. India is a good test case for this new approach due to its large amount of $SO_2$ emissions and a large number of point sources. In Section 2, we list the datasets used in this study. In Section 3 we explain the methodology, including how emission spreading occurs and how our deconvolution algorithm works. In Section 4 we present the validation of our method using model results and show the improved $SO_2$ emission results for India. Finally, we conclude with a discussion of the limitations and potential applications of our algorithm in section 5.

## 2 Datasets

### 2.1 Satellite observations and wind field datasets

The flux is derived by multiplying TROPOMI measured $SO_2$ vertical column density (VCD) gradients with the horizonal 2D wind field. The divergence of this flux is related to the emissions. We estimate emissions using the TROPOMI COBRA (Covariance-Based Retrieval Algorithm) $SO_2$ product with a spatial resolution of (3.5 km × 5.5 km at nadir). The COBRA retrievals can detect small anthropogenic sources with emissions of 8.0 Gg $year^{-1}$(Theys et al., 2021). Specifically, we calculate the $SO_2$ divergence for the period December 2018 to November 2023. To ensure good data quality, we exclude pixels with a QA value below 0.5 or a surface height above 3 km. (https://data-portal.s5p-pal.com/product-docs/SO2cbr/S5P-BIRA-PRF-SO2CBR_1.0.pdf, last access: 31 July, 2025). Daily wind fields are taken from the daily operational 12h forecasts of the European Centre for Medium-range Weather Forecasts (ECMWF) at 0.25° × 0.25° resolution (https://www.ecmwf.int/en/forecasts, last access: 31 July, 2025) and interpolated at the mid-point of the Planetary Boundary Layer (PBL). Although the divergence is calculated for each day, we average it over each season to generate a relatively low-noise $SO_2$ emission inventory.

### 2.2 Copernicus Atmospheric Monitoring Service (CAMS) datasets

The monthly mean OH climatology is derived from the 5-year averaged from November 2018 to December 2023 using CAMS (Copernicus Atmospheric Monitoring Service) global forecast data (https://ads.atmosphere.copernicus.eu, last access: 9 September, 2025) for chemical lifetime calculation. The forecast dataset is based on ECMWF's Integrated Forecast System (IFS), which assimilates and models the concentrations of more than 50 chemical species (such as $SO_2$ and OH), seven aerosol types, and various meteorological factors, all at a resolution of 0.4° × 0.4°. We derive the monthly mean OH climatology for the time period before the TROPOMI overpass time (13:30PM local time) by averaging monthly OH concentration at 6:00AM UTC (11:30AM local time) within the PBL between 2018 to 2023, excluding days with extreme weather events, such as large-scale precipitation. The dry deposition lifetime is calculated by assuming a constant dry deposition velocity of 0.4 cm $s^{-1}$ in the atmosphere. Except for OH concentration, the $SO_2$ VCD within PBL and the wind field data in the mid-PBL layer from CAMS datasets are used for the method validation in Section 4.1.

https://doi.org/10.5194/egusphere-2025-4490
Preprint. Discussion started: 24 September 2025


### 2.3 $SO_2$ point source inventories for India

We use two datasets to validate the accuracy of the location of our detected $SO_2$ point sources. The first resource is from the global power plants database maintained by World Resources Institute, which is available at https://github.com/wri/global-power-plant-database (last access: 31 July, 2025). This database includes in total 255 coal-based thermal power plants in India. They are used for comparison with our detected point sources. The second resource is the global catalog of large $SO_2$ point sources from the Multi-Satellite Air Quality Sulfur Dioxide ($SO_2$) database, Long-Term L4 Global V2 (referred to as MSAQS$O_2$L4) (Fioletov et al., 2023). This catalog is based on $SO_2$ slant column density (SCD) data from two sources: the operational version 2 OMI and OMPS Principal Component Analysis (PCA) retrieval algorithm (Li et al., 2020), and the TROPOMI Covariance-Based Retrieval Algorithm (COBRA) (Theys et al., 2021). Their emission estimates are derived using an exponentially modified plume fitting model. In total, the catalog identifies 92 $SO_2$ point sources in India.

## 3 Methodologies

### 3.1 Spreading effect (Chen et al., 2025) of $SO_2$ divergence calculation on different spatial scales

Since the data used for the divergence calculation, TROPOMI $SO_2$ measurements and 2D wind fields, are gridded rather than continuous, we calculate the $SO_2$ divergence using the second-order central difference method. The total divergence is a superposition of components in both the *x* and *y* directions; for simplicity, we present the calculation along the *x* direction only. Specifically, the $SO_2$ divergence of grid cell *i* in the *x* direction can be calculated as follows:

$$D_{x(i)} = \frac{F_{x(i+1)} - F_{x(i-1)}}{2\Delta x} \quad (1)$$

$$F_{x(i+1)} = w_{x(i+1)} \cdot V_{(i+1)} \quad (2)$$

$$F_{x(i-1)} = w_{x(i-1)} \cdot V_{(i-1)} \quad (3)$$

$D_{x(i)}$ is the divergence in grid cell *i* calculated along the *x* direction. $F_{x(i)}$ denotes the flux of $SO_2$ in grid cell *i* along the *x* direction. $\nabla x$ is the resolution of the grid-scale. $w_{x(i)}$ represents the wind in grid cell *i* along *x* direction. $V_i$ is $SO_2$ VCD in grid cell *i*. The total divergence for each grid cell equals the sum of the divergence along *x* and *y* directions.

There is a discretization in this divergence calculation leading to the spreading of the calculated point source emissions. Specifically, Eq. (1) can be rewritten as:

$$D_{x(i)} = \frac{1}{2}\left[\frac{(F_{x(i+1)} - F_{x(i)})}{\Delta x} + \frac{(F_{x(i)} - F_{x(i-1)})}{\Delta x}\right] \quad (4)$$

This can further be expressed as:

$$D_{x(i)} = \frac{1}{2}[D_{RE(i)} + D_{LE(i)}], \quad (5)$$

where $D_{RE(i)}$ and $D_{LE(i)}$ denotes the divergence at the right and left edges of grid cell *i*, respectively. Hence, the divergence of each grid cell can be viewed as a linear interpolation of the divergence in its surrounding regions. This causes the spreading of point source emissions.

We use Eq. (1) to calculate gridded $SO_2$ divergence at different spatial resolutions to determine the optimal resolution for emissions, which minimize both spreading effect and the noise level. The target spatial resolutions from coarse to fine are 0.1° × 0.1°, 0.05° × 0.05°, 0.025° × 0.025°, and 0.01° × 0.01°. Table 1 shows the six investigated divergence calculations using the mentioned resolutions and two calculation strategies. Either the divergence is first calculated on the TROPOMI pixels and then interpolated to the target resolution (option 1) or the $SO_2$ VCD is first interpolated to the target resolution, and then the divergence is calculated (option 2). The $SO_2$ emission results of these six cases are shown in Fig. 1.

https://doi.org/10.5194/egusphere-2025-4490
Preprint. Discussion started: 24 September 2025


**Table 1. $SO_2$ emissions on different spatial scales**

| Case name | Method (1. Divergence calculation on TROPOMI pixels, 2. Divergence calculation on regular grid cells) | Spatial resolution |
|---|---|---|
| 0.1°_Regular Grid | 2 | 0.1° × 0.1° |
| 0.05°_Regular Grid | 2 | 0.05° × 0.05° |
| 0.025°_Regular Grid | 2 | 0.025° × 0.025° |
| 0.025°_TROPOMI Pixel | 1 | 0.025° × 0.025° |
| 0.01°_Regular Grid | 2 | 0.01° × 0.01° |
| 0.01°_TROPOMI Pixel | 1 | 0.01° × 0.01° |

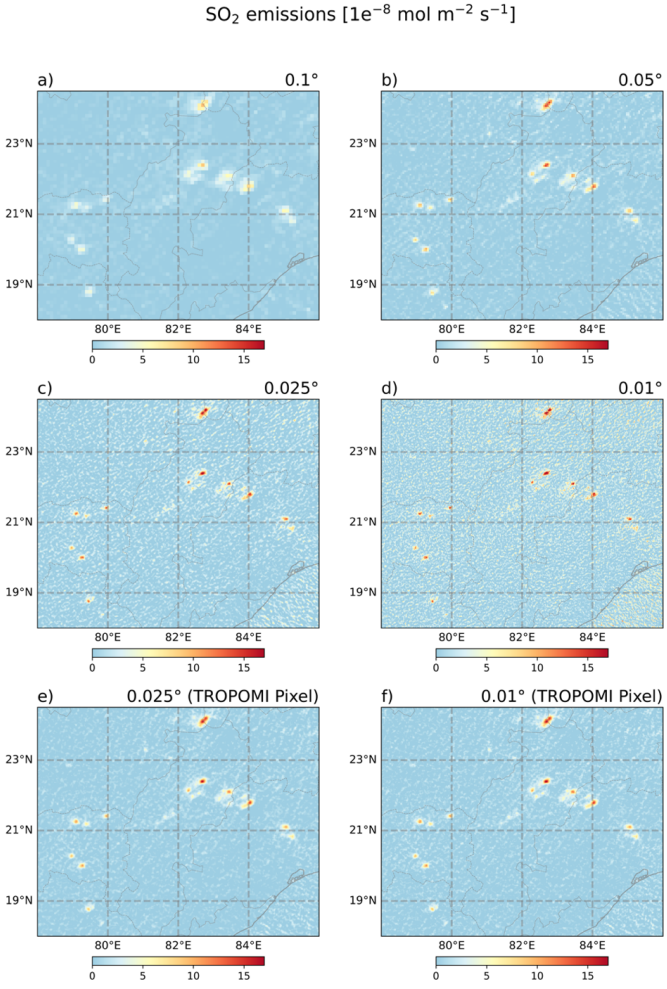


**Figure 1. Annual mean $SO_2$ emissions during December 2022 to November 2023 on different spatial resolutions in a region of India with strong emission sources. The cases are shown for a) 0.1°_Regular Grid, b) 0.05°_Regular Grid, c) 0.025°_Regular Grid, d) 0.01°_Regular Grid, e) 0.025°_TROPOMI Pixel, and f) 0.01°_TROPOMI Pixel.**

https://doi.org/10.5194/egusphere-2025-4490
Preprint. Discussion started: 24 September 2025


In Fig. 1a-d, the $SO_2$ divergence is calculated directly on regular grids in the target resolutions. In Fig. 1a-c, as the grid resolution becomes finer, the $SO_2$ emission map shows more details, indicating the emission resolution also becomes finer. The higher grid resolution can reduce the spreading effect caused by the linear interpolation of divergence calculation and thus improve the emission resolution, while the noise level increases due to the finer resolution. However, when the grid resolution becomes finer than the TROPOMI pixel size, i.e. the grid resolution changes from 0.025° × 0.025° to 0.01° × 0.01° as shown in Fig.1c and d, the improvement on emission resolution becomes minimal and the noise levels are still increasing. In this case, the TROPOMI pixel size becomes the limiting factor, and further increasing the grid resolution does not improve the effective emission resolution but increase the noise. When the resolution matches the resolution of Fig. 1c (0.025° × 0.025°) and d (0.01° × 0.01°), while the divergence is first calculated on the TROPOMI pixel as shown in Fig. 1e and f, the noise levels are efficiently reduced. The effective emission resolution between Fig. 1e and 1f are comparable, indicating that increasing the grid resolution no longer improves the effective emission resolution in this case. Nonetheless, some spreading of point-source emissions always remains, constrained either by the grid or the TROPOMI pixel size. In the next section, we will introduce a method to further improve the emission resolution on any given grid cell resolution. Fig. 1e and 1f have less noise compared to Fig. 1c and 1d, making it easier to distinguish point sources from the noise. Since the emission resolution in Fig. 1e (0.025°) and Fig. 1f (0.01°) are similar, we will use the $SO_2$ emissions from Fig. 1e (0.025°) as the baseline in the following sections. The effective resolution will be analyzed in Section 3.2.2.

## 3.2 Development of a sharpening algorithm

### 3.2.1 Deconvolution algorithm

Since the spreading of emissions always takes place, we explore a deconvolution method to further improve the emission resolution. We can use a spreading kernel $\boldsymbol{B}$ to describe how the original emission map $\boldsymbol{X}$ spreads to form the blurred emission map $\boldsymbol{Y}$ as expressed in the following equation:

$$\boldsymbol{Y} = \boldsymbol{B} * (\boldsymbol{X} + \varepsilon), \tag{6}$$

where $e$ represents the noise in the original $SO_2$ emission map $\boldsymbol{X}$. Now, we use the spreading kernel to calculate the sharpening kernel. When requiring local mass balance, the sharpening kernel $\boldsymbol{A}$ used to reconstruct each point source emissions can be expressed by:

$$\boldsymbol{A} = \boldsymbol{I} + (\boldsymbol{I} - \boldsymbol{B})\, b_{00}^{-1}, \tag{7}$$

where $b_{00}$ is the central element of the kernel $\boldsymbol{B}$, and $\boldsymbol{I}$ is the identity function. We cannot apply this sharpening kernel to the whole map $\boldsymbol{Y}$ because this would also sharpen spread emissions and increase the noise. Therefore, we define the following "local" sharpening kernel $\boldsymbol{A}'$

$$\boldsymbol{A}' = \begin{cases} \boldsymbol{A} & at\ (i,j) \\ \boldsymbol{I} & elsewhere \end{cases}, \tag{8}$$

In each iteration $n$, we select the location $(i, j)$ with the highest remaining emission in emission map $Y_{n-1}$, which has not been selected in previous iterations. The updated emission map is then computed as:

$$\boldsymbol{Y_n} = \boldsymbol{Y_{n-1}} \times \boldsymbol{A}' \tag{9}$$

Note that in typical deconvolution method, the sharpening kernel is applied to the entire region at once. However, in our approach, sharpening in this way causes the point source emissions to add more noise as shown in Fig. 2a. We therefore use Eq. 9 to sharpen locations stepwise by using the local sharpening kernel of Eq. 8 for locations in a descending order of emission strength (from high to low), minimizing the risk of applying sharpening to regions dominated by the spread emissions or noise. There is total mass balance in each local area where deconvolution is applied.

https://doi.org/10.5194/egusphere-2025-4490
Preprint. Discussion started: 24 September 2025


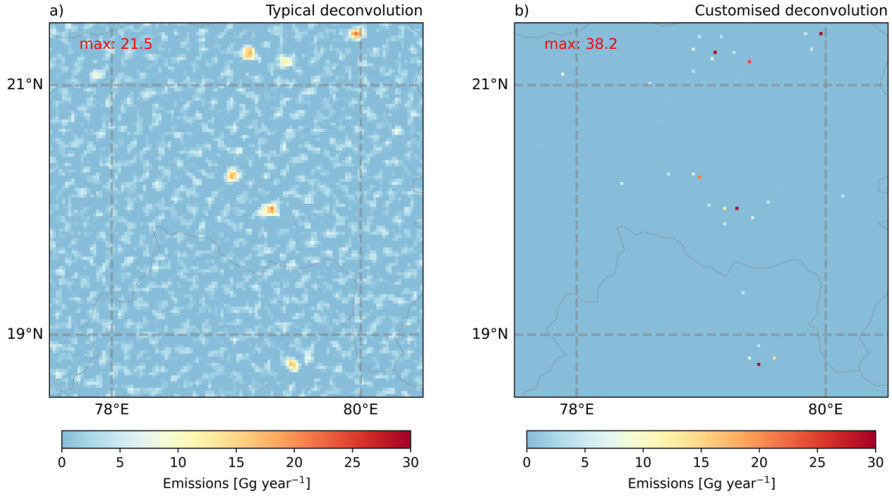


**Figure 2. $SO_2$ emissions of a zoom-in region in India. a) $SO_2$ emissions after the typical deconvolution. b) $SO_2$ emissions after customized deconvolution (sharpening applied in descending order of emission)**

The iterations process stops when the highest unsharpened value $\boldsymbol{Y_{n-1(i,j)}}$ is below the noise level in $\boldsymbol{Y}$. This means we only sharpen emissions above the noise level. This approach helps focusing on real point source emissions. If values below the noise level are sharpened, it will amplify the noise, making it harder to distinguish real point source from the sharpened noise. Figure 3 compares the results of sharpening emissions above zero and above noise level. In Fig. 3a, where all above zero grids are sharpened, the noise is also amplified.

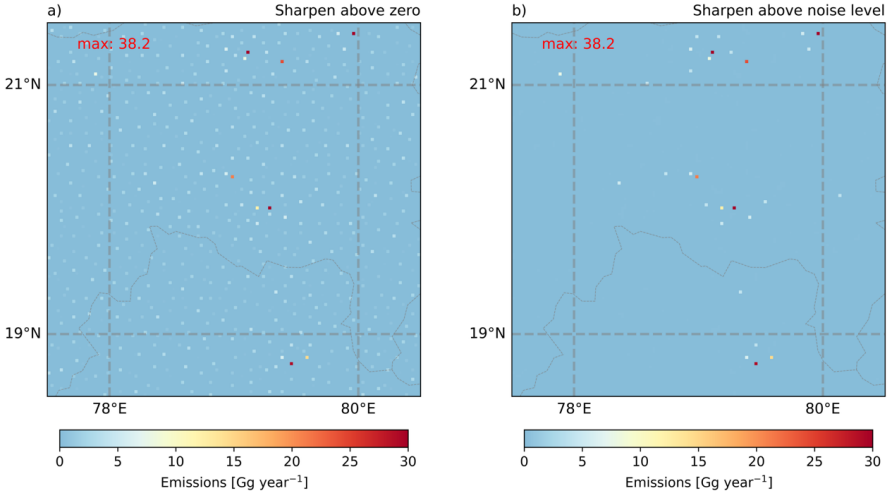


**Figure 3. $SO_2$ emissions of a zoom-in region in India. a) $SO_2$ emissions sharpened down to all non-zero values. b) $SO_2$ emissions sharpened only above the noise level.**

https://doi.org/10.5194/egusphere-2025-4490
Preprint. Discussion started: 24 September 2025


### 3.2.2 Determination of the spreading kernel

The spreading kernel ***B*** is used to understand and quantify how point source emissions spread to its surrounding areas. Ideally, the $SO_2$ emission signal appears only at the point source location. Emissions in the grid cells adjacent to the source location can be considered as spread emissions. Figure 4 shows the variation of $SO_2$ emissions with distance from the point source locations for all emission cases in Table 1. To obtain a spreading kernel which represents the overall spreading pattern of point source emissions, we fit the emission variation around the large and isolated point sources in India using a Gaussian-shaped function. Figure 4a shows the $SO_2$ emissions and the corresponding Gaussian-shaped fitting functions varies with distance in kilometers (x axis). From Fig. 4a, we draw similar conclusions to those from Fig. 1: as the spatial resolution becomes finer, the emission resolution improves. But when the grid resolution becomes finer than the TROPOMI pixels, the improvement in emission resolution becomes marginal. This is because the TROPOMI pixel, rather than the divergence method, becomes the dominating factor in spreading point source emissions. The TROPOMI pixel represents the finest spatial resolution achievable for emission resolution. Figure 4b also shows the $SO_2$ emission variation with the distance from the point source location, where distance is expressed in grid cells (x axis). This is to know the spreading pattern in grid-cell scale to define the gridded deconvolution sharpening kernel, which then can be applied to sharpen gridded $SO_2$ emissions. Since we decide to derive the $SO_2$ emissions based on TROPOMI pixels and regrided to 0.025° afterwards, we derive the spreading pattern from the corresponded Gaussian-shaped function (red dots in Fig. 4b). The $SO_2$ emissions of point sources approaches zero at approximately 4 grid cells (around 11.25 km) away from the point sources. Therefore, we define the spreading region for each point source as a 9 × 9 grid cells (around 22.5 km × 22.5 km) centered on the source location. Note that Fig. 4 is based on one year of data, from December 2022 to November 2023, to show the spreading pattern of emission at different resolutions. The final spreading kernel is derived from a 5-year average (from December 2018 to November 2023) of $SO_2$ emissions of 0.025° TROPOMI pixel case. The derived kernel ***B*** is a Gaussian-shaped function with a sigma of 1.83 grid cells. (See details in Section S1 in supplementary file)

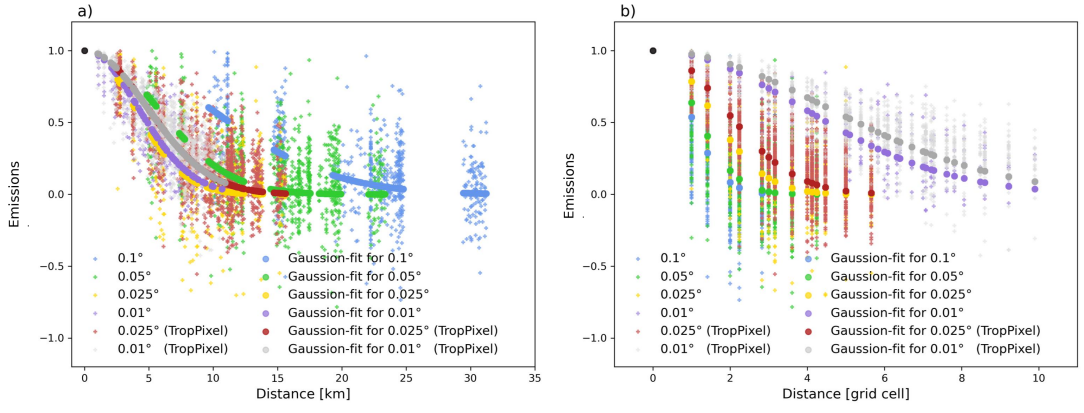


**Figure 4. Variation of normalized $SO_2$ emissions with distance from the point source location, and the corresponding Gaussian-shaped fitting functions. The $SO_2$ emissions are averaged within December 2022 to November 2023. The emission distributions of 62 large and isolated point sources are used for fitting. The black point at (0,1) represents the location of the point source. The spreading of $SO_2$ emissions is fitted for the six cases in Table 1.**

https://doi.org/10.5194/egusphere-2025-4490
Preprint. Discussion started: 24 September 2025


## 4 Results and discussions.

Previous studies have shown the effectiveness of the divergence method in estimating emissions. We expect a further improvement combining the divergence method with our deconvolution algorithm. To evaluate the performance of the combined approach, we implement it within a closed-loop validation process. Specifically, we apply the divergence method together with the deconvolution algorithm to derive $SO_2$ emissions based on simulation results from the CAMS model, including $SO_2$ column densities, OH concentrations and IFS model-output wind fields. Since the input emission used to drive the CAMS model is known, we can assess the accuracy of our method by comparing the derived top-down emissions with the original model input. Figure 5 shows the comparison between the model input $SO_2$ emissions and the top-down emissions. There is a noticeable difference in distribution between the model input emissions in Fig. 5a and the emissions derived only from the classic divergence method (CDM) in Fig. 5b. The latter emission map appears more dispersed, with the point source emissions spreading into adjacent grid cells. This spreading effect also leads to a lower emission peak at the point source location, for example, the maximum value is lower in Fig. 5b than in Fig 5a. In contrast, the model input emissions in Fig. 5a are more concentrated, showing a higher value directly at the point source. To reduce this discrepancy, we sharpen Fig. 5b with a model-based 5×5 sharpening kernel. The size and the shape of this kernel are derived from the spreading pattern (Fig. S2) of "blurry" emissions (Fig. 5b) using Eq. 7. The emissions after sharpening in Fig. 5c prove that the deconvolution algorithm effectively improves the emission estimates. The total emissions shown in Fig. 5b and 5c are the same and comparable to 5a. Additionally, Fig. 6 compares the $SO_2$ emission amount of point sources across three different inventories. As shown in Fig. 6a, a clear underestimation is shown for $SO_2$ emissions derived only with the divergence method. But the underestimation is efficiently reduced after applying the sharpening as seen in Fig. 6b. It is important to note that the CAMS model resolution is relatively coarse (0.4° × 0.4°). At this resolution, some individual emissions are not well recovered in Fig. 6b, because the spreading regions of the 5×5 kernels can overlap with nearby point sources. Applying this combined approach to real measurements with finer spatial resolution will lead to a better performance, which will be shown in the following results.

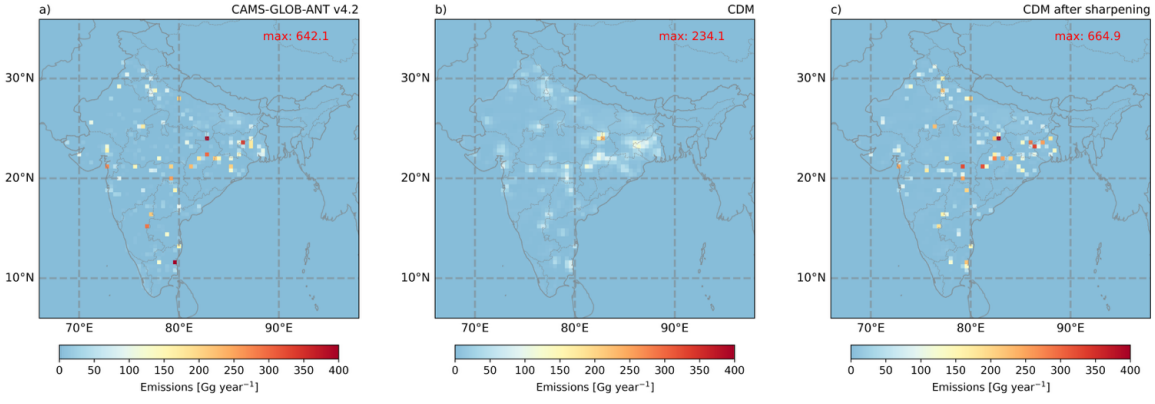


**Figure 5. $SO_2$ emissions distribution averaged within December 2019 and November 2020. a) CAMS emission inventory. b) $SO_2$ emissions calculated through classic divergence method (CDM). c) divergence method after sharpening using a 5 × 5 kernel.**

https://doi.org/10.5194/egusphere-2025-4490
Preprint. Discussion started: 24 September 2025


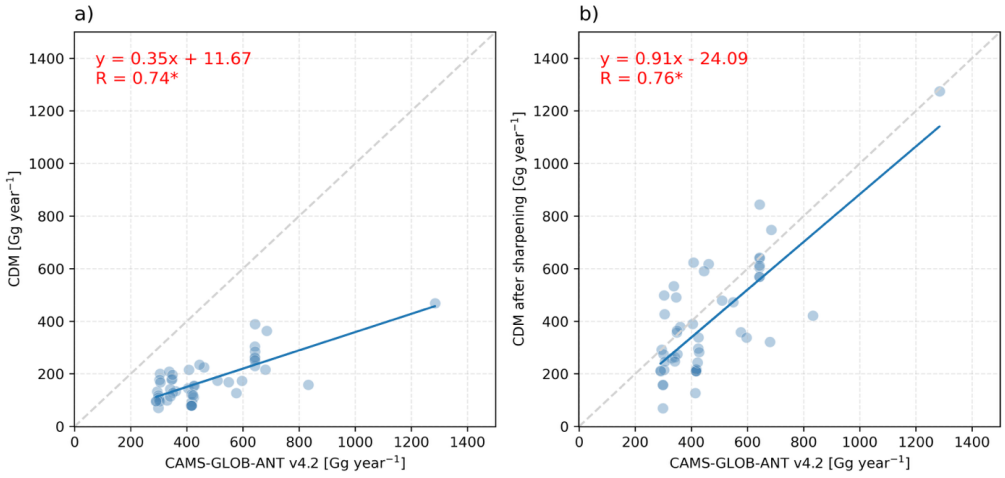


**Figure 6. Comparison of $SO_2$ point source emissions between model input inventory (CAMS-GLOB-ANT v4.2, x axis) and model-based top-down estimate (y axis). The largest 50 point source emissions in CAMS-GLOB-ANT v4.2 are used in this comparison. a) y axis represents the top-down emissions derived from classic divergence method (CDM). b) y axis represents the top-down emissions from CDM sharpened by the 5 × 5 kernel. Since the top-down emission signal may be spatially shifted, the sum of emissions from two grid cells is used for comparison: one corresponding to the point source location and the other to the grid cell with the maximum emissions in the surrounding area.**

After the model-based evaluation, we apply the deconvolution algorithm to satellite-based top-down $SO_2$ emissions at a resolution of 0.025° × 0.025°. At this high resolution, the emission signals of point sources are not easily visible on the large map over India. To better illustrate the improvement, we select the 79 $SO_2$ point sources from $SO_2$ catalog MSAQSO$_2$L4 and check their emission distribution at surrounding areas (9 × 9 grid cell areas) before and after sharpening. The locations are shown in Table S1. We average the emission distributions centered on these 79 point sources for each surrounding grid cell, with the results shown in Fig. S2. In Fig S2a, we see that the actual emission distribution before sharpening closely follows a 2D Gaussian pattern. This supports the Gaussian-shaped spreading pattern derived earlier from Fig. 4b. Figure S2b shows the distribution after sharpening, where the emission spread is removed and the point source emissions are enhanced by up to 20 times compared to the unsharpened case, while ensuring mass conservation. The emission signal becomes more concentrated into a single grid cell, effectively increasing the emission resolution to match the grid cell resolution. In addition to this averaged analysis, we also check the emission distribution of several individual point sources. In Fig. 7 four examples are given to show the effect of the sharpening in individual cases, the left figure shows the original distribution and the right figure after sharpening for an area of 9 × 9 grid cells. In Fig. 7a, the emissions of two sources are mixed before sharpening, but they are clearly separated in Fig. 7b. In Fig. 7c–f, a strong signal appears at the main source location, with smaller sources also visible, reflecting that power-station chimneys are not concentrated in a single location. In Fig. 7g and 7h, the point source emissions are much lower than in the previous examples, the emission distribution before sharpening shows less the characteristics of a Gaussian shape, making it more difficult to identify. However, after applying the sharpening algorithm the emission source is clearly identified and quantified.

https://doi.org/10.5194/egusphere-2025-4490
Preprint. Discussion started: 24 September 2025


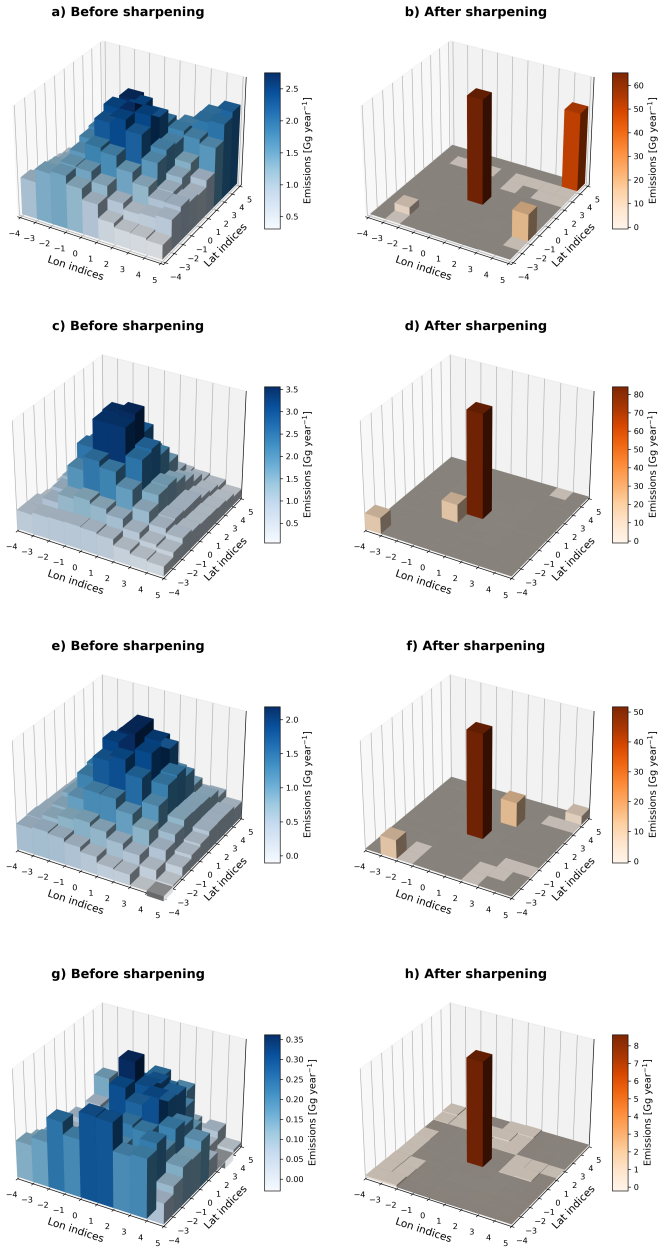


**Figure 7. $SO_2$ emission distribution centered on a $SO_2$ point source within a 9 × 9 grid cell area. The left column represents the $SO_2$ emission before sharpening and the right column represents the emission after sharpening. a) and b): Vindhyachal Super Thermal Power Station (24.090°N, 82.675°E), with Renusagar Power Station (24.182°N, 82.793°E) located in the top-right corner of this 9 × 9 grid cell area. c) and d): The expansion of Neyveli Power station (11.555°N, 79.444°E). e) and f): Vedanta Aluminum Captive Power Plant (21.788°N, 84.055°E). g) and h): Sri Damodaram Sanjeeraiah Thermal Power Station (14.829°N, 80.126°E).**

https://doi.org/10.5194/egusphere-2025-4490
Preprint. Discussion started: 24 September 2025


The improved emission resolution makes it easier to precisely locate the $SO_2$ point sources in the top-down emission inventory. To evaluate the location accuracy of the $SO_2$ point sources in our emission inventory, we compare the detected locations with the actual locations of 79 known point sources as shown in Fig. 8. The locations of the selected point sources are shown in Table S1. Among them, 56 point sources are detected within the same grid cell as their actual location, and 20 point sources are detected in the grid cells directly adjacent to the actual locations. If we consider the smallest TROPOMI pixel size (3.5 km × 5.5 km at nadir) as the minimum resolution for detecting point sources, then 76 out of 79 point sources (approximately 96%) are successfully located within this range using emissions derived from TROPOMI measurements. The remaining 3 point sources are detected two grid cells away from their actual locations, which is the result of the influence from nearby sources, e.g. other closely located point sources or large urban areas, may cause the peak VCD and resulting emissions shift away from the point source location.

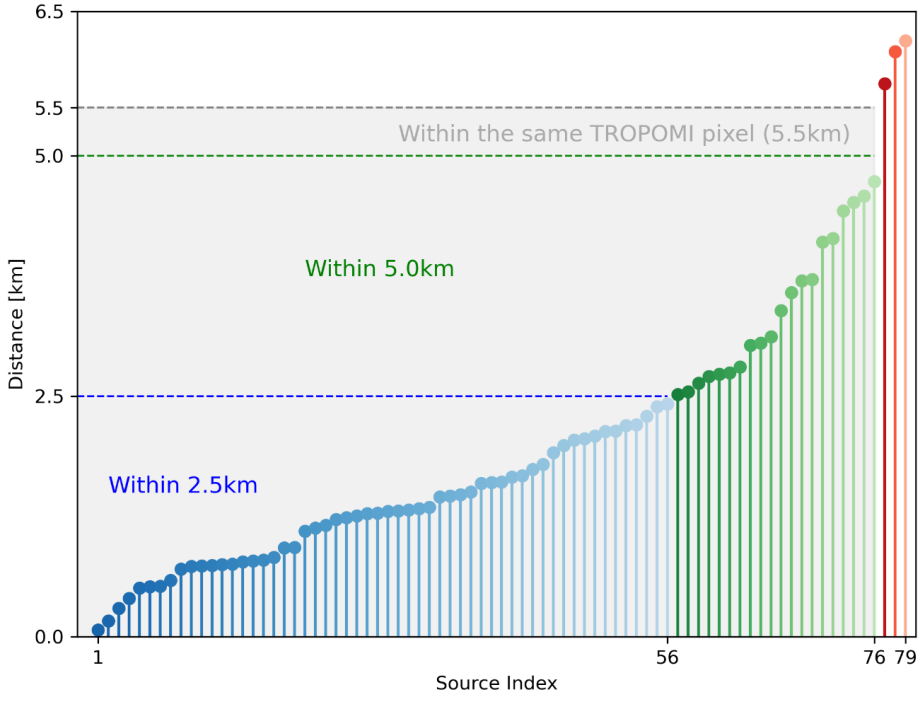


**Figure 8. Distance between the actual and our detected locations of large Indian $SO_2$ point sources. The grid resolution of the emissions is 0.025° × 0.025° (approximately 2.5 km × 2.5 km per grid cell). Blue dots below 2.5 km: Detected and actual locations fall within the same grid cell. Green dots between 2.5 km and 5.0 km: Detected locations are in grid cells directly adjacent to the actual locations. Red dots above 5.0 km: Detected locations are in grid cells that are one grid cell further away from the actual locations. Gray shadow below 5.5 km: Detected and actual locations fall within the same TROPOMI pixel (3.5 km × 5.5 km at nadir).**

Since the point source emission signals have been enhanced, we expect more emission signals to be visible on our satellite-based emission map. Coal-based power plants are the largest sector for $SO_2$ emissions in India. To assess our results, we compare the emission signals detected in this study with the actual locations of all coal-based power plants across the country. These plants have capacities ranging from 10 MW to 4760 MW annually. Given the high resolution of our emission data and the fact that emission peaks may not align exactly with plant locations, we consider a power plant "detected" if there is any emission signal above 3.4 Gg $year^{-1}$ within 6 km (the average TROPOMI footprint size) of the plant (See more information of noise level in Fig. S3). The results summarized in Table 2 shows that approximately 80% of power plants with capacities

https://doi.org/10.5194/egusphere-2025-4490
Preprint. Discussion started: 24 September 2025


larger than 100 MW per year are successfully detected, while the emissions of the remaining 20% of power plants are lower than the noise level. These detected plants represent 99% of India's total coal-based power generation. For large power plants with annual capacities above 1000 MW, contributing 77% of the total generation, the detection rate reaches 95%. The higher the output, the more coal is burned, making emissions more likely to be detected.

**Table 2. Comparison between the India coal-combustion thermal power plants and point source emission signal in this study**

| Power Generation | Amount of power plants | Amount of detected power plants | Detection rate |
|---|---|---|---|
| >= 1500 MW | 38 | 38 | 100% |
| >= 1000 MW | 94 | 89 | 95% |
| >= 500 MW | 147 | 123 | 84% |
| >= 200 MW | 176 | 141 | 80% |
| >= 100 MW | 186 | 147 | 79% |
| All | 255 | 156 | 61% |

We also find some new $SO_2$ point sources based on our satellite-based $SO_2$ emission map. These emissions are not included in the Indian power plant database and also are not identified by other top-down $SO_2$ catalogs. These new point sources include not only coal-based power plants but also cement factories, a crude oil production facility, and copper industry. Table 3 shows a list of these newly detected point sources and their locations.

**Table 3. Newly detected $SO_2$ point sources in India**

| Number | State | Position | Name |
|---|---|---|---|
| 1 | GUJARAT | （23.498°N, 68.578°E） | Adani Cements plants |
| 2 | | （21.560°N, 72.923°E） | Ankleshwar CTF ONGC (Gasoline industry) |
| 3 | | （21.704°N, 72.542°E） | Birla Copper industry |
| 4 | | （22.317°N, 69.845°E） | Sez Pcg Reliance Refinery |
| 5 | MADHYA PRADESH | (22.064°N, 75.859°E) | NTPC Power plant |
| 6 | MAHARASHTRA | (17.558°N, 75.981°E) | NTPC Power plant |
| 7 | ODISHA | （20.891°N, 84.989°E） | JSPL Angul Captive Power Plant |

## 5 Conclusion

In this study, we developed a deconvolution algorithm to improve the resolution of $SO_2$ emissions estimated using the flux-divergence method and TROPOMI satellite data. Before applying the algorithm, emissions from point sources tend to spread,

https://doi.org/10.5194/egusphere-2025-4490
Preprint. Discussion started: 24 September 2025


making it difficult to detect smaller sources or distinguish closely located sources. After applying the deconvolution, the emission signals become sharper and more concentrated at their true locations. On average, emissions at point source locations increase by up to 20 times compared to before the sharpening at a resolution of 0.025° × 0.025°. This sharpening helps to separate emissions from nearby sources. To validate the results, we compared our results with the locations of 79 $SO_2$ sources in India identified by Fioletov et al. (2023). We find that 96% of the detected sources fall within the same TROPOMI pixel as their real locations. We detected about 80% of all coal power plants with power generation larger than 100 MW per year, which account for 99% of India's total coal-based electricity generation. With the improved signal, we also identified 7 new point sources not previously reported. These include coal power plants, copper and cement industries, and a crude oil facility. However, there are some limitations. If a point source is located near the edge or corner of a grid cell, the signal may be shifted to an adjacent grid cell. So, to estimate actual emissions, we still recommend summing emissions over a small area around the point source. Although this algorithm is developed for $SO_2$, it can also be applied to other pollutants emitted by point sources like $NO_x$. It helps sharpen emission signals on existing grid cells and is a useful step toward building accurate emission inventories.

**Data availability:**

The TROPOMI Level-2 COBRA $SO_2$ data created by the Royal Belgian Institute for Space Aeronomy (BIRA-IASB) are publicly available on the PAL website https://data-portal.s5p-pal.com/products/SO2cbr.html (Theys, 2024a) and the BIRA website https://distributions.aeronomie.be (Theys, 2024b). The daily operational 12h forecast wind field data are available at https://www.ecmwf.int/en/forecasts/datasets/open-data (European Centre for Medium-Range Weather Forecasts (ECMWF), 2024). CAMS global atmospheric composition forecast data are available with a login account on the Copernicus website https//ads.atmosphere.copernicus.eu/datasets/cams-global-atmospheric-composition-forecasts?tab=overview, (Copernicus Atmospheric Monitoring Service (CAMS), 2024). $SO_2$ global catalog MSAQ$SO_2$L4 data are available on the NASA Goddard Earth Sciences (GES) Data and Information Services Center (DISC) website https://doi.org/10.5067/MEASURES/SO2/DATA406 (Fioletov, 2022). Indian power plant locations from the global power plant database maintained are available from https://github.com/wri/global-power-plant-database (World Resources Institute (WRI), 2021)

**Author contribution**

**YC** carried out the formal analysis and writing**. RJA** provided mathematical and technical support for the deconvolution, contributed to the conceptualization, and assisted with reviewing and editing the paper**. JD** contributed to the conceptualization and was involved in reviewing and editing the paper**. HE** contributed through reviewing and editing the paper**. FC** verified the deconvolution on $NO_x$ emissions**. PFL** contributed through regular discussions, provided advice, and assisted with reviewing and editing the paper.

**Competing interests**

The authors declare that they have no conflict of interest.

**Financial support**

We acknowledge the funding from the China Scholarship Council (CSC).

**Acknowledgements**

We acknowledge the team of ECMWF, Copernicus Project, and all the other investigators who have made the data used in this study and made them available online.

https://doi.org/10.5194/egusphere-2025-4490
Preprint. Discussion started: 24 September 2025


**References:**

Arnold, F.: Atmospheric Aerosol and Cloud Condensation Nuclei Formation: A Possible Influence of Cosmic Rays?, SSRv, 125, 169-186, 10.1007/s11214-006-9055-4, 2006.

Beirle, S., Borger, C., Dörner, S., Eskes, H., Kumar, V., de Laat, A., and Wagner, T.: Catalog of NOx emissions from point sources as derived from the divergence of the NO2 flux for TROPOMI, Earth Syst. Sci. Data, 13, 2995-3012, 10.5194/essd-13-2995-2021, 2021.

Beirle, S., Borger, C., Dörner, S., Li, A., Hu, Z., Liu, F., Wang, Y., and Wagner, T.: Pinpointing nitrogen oxide emissions from space, Sci. Adv., 5, eaax9800, doi:10.1126/sciadv.aax9800, 2019.

Bhargava, S. and Bhargava, S.: Ecological consequences of the acid rain, IOSR J. Appl. Chem, 5, 19-24, 2013.

Bovensmann, H., Burrows, J. P., Buchwitz, M., Frerick, J., Noël, S., Rozanov, V. V., Chance, K. V., and Goede, A. P. H.: SCIAMACHY: Mission Objectives and Measurement Modes, J. Atmos. Sci., 56, 127-150, https://doi.org/10.1175/1520-0469(1999)056<0127:SMOAMM>2.0.CO;2, 1999.

Brasseur, G. P. and Jacob, D. J.: Modeling of Atmospheric Chemistry, Cambridge University Press, Cambridge, DOI: 10.1017/9781316544754, 2017.

Callies, J., Corpaccioli, E., Eisinger, M., Hahne, A., and Lefebvre, A.: GOME-2-Metop's second-generation sensor for operational ozone monitoring, ESA Bull., 102, 28-36, 2000.

Central Electricity Authority: CEA Annual Report 2022–23, Ministry of Power, Government of India, New Delhi, 2023.

Chakraborty, N., Mukherjee, I., Santra, A. K., Chowdhury, S., Chakraborty, S., Bhattacharya, S., Mitra, A. P., and Sharma, C.: Measurement of CO2, CO, SO2, and NO emissions from coal-based thermal power plants in India, Atmos. Environ., 42, 1073-1082, https://doi.org/10.1016/j.atmosenv.2007.10.074, 2008.

Chan, C. and Delina, L. L.: Energy poverty and beyond: The state, contexts, and trajectories of energy poverty studies in Asia, Energy Res. Soc. Sci, 102, 103168, 2023.

Chen, Y., van der A, R. J., Ding, J., Eskes, H., Williams, J. E., Theys, N., Tsikerdekis, A., and Levelt, P. F.: SO2 emissions derived from TROPOMI observations over India using a flux-divergence method with variable lifetimes, Atmos. Chem. Phys., 25, 1851-1868, 10.5194/acp-25-1851-2025, 2025.

Cifuentes, F., Eskes, H., Dammers, E., Bryan, C., and Boersma, F.: Accurate space-based NOx emission estimates with the flux divergence approach require fine-scale model information on local oxidation chemistry and profile shapes, Geosci. Model Dev., 18, 621-649, 10.5194/gmd-18-621-2025, 2025.

Copernicus Atmospheric Monitoring Service (CAMS): CAMS global atmospheric composition forecast data [data set] [dataset], 2024.

Crippa, M., Guizzardi, D., Pagani, F., Schiavina, M., Melchiorri, M., Pisoni, E., Graziosi, F., Muntean, M., Maes, J., Dijkstra, L., Van Damme, M., Clarisse, L., and Coheur, P.: Insights into the spatial distribution of global, national, and subnational greenhouse gas emissions in the Emissions Database for Global Atmospheric Research (EDGAR v8.0), Earth Syst. Sci. Data, 16, 2811-2830, 10.5194/essd-16-2811-2024, 2024.

Eisinger, M. and Burrows, J. P.: Tropospheric sulfur dioxide observed by the ERS-2 GOME instrument, Geophys. Res. Lett., 25, 4177-4180, https://doi.org/10.1029/1998GL900128, 1998.

European Centre for Medium-Range Weather Forecasts (ECMWF): Daily operational 12 h forecast wind field data [data set] [dataset], 2024.

Feldman, L., Maibach, E. W., Roser-Renouf, C., and Leiserowitz, A.: Climate on cable: The nature and impact of global warming coverage on Fox News, CNN, and MSNBC, The International Journal of Press/Politics, 17, 3-31, 2012.

Fioletov, V., McLinden, C. A., Griffin, D., Abboud, I., Krotkov, N., Leonard, P. J. T., Li, C., Joiner, J., Theys, N., and Carn, S.: Multi-Satellite Air Quality Sulfur Dioxide (SO2) Database Long-Term L4 Global V2 [data set] [dataset], 10.5067/MEASURES/SO2/DATA406, 2022.

https://doi.org/10.5194/egusphere-2025-4490
Preprint. Discussion started: 24 September 2025


Fioletov, V. E., McLinden, C. A., Krotkov, N., and Li, C.: Lifetimes and emissions of SO2 from point sources estimated from OMI, Geophys. Res. Lett., 42, 1969-1976, 10.1002/2015gl063148, 2015.

Fioletov, V. E., McLinden, C. A., Krotkov, N., Moran, M. D., and Yang, K.: Estimation of SO2 emissions using OMI retrievals, Geophys. Res. Lett., 38, https://doi.org/10.1029/2011GL049402, 2011.

Fioletov, V. E., McLinden, C. A., Krotkov, N., Li, C., Joiner, J., Theys, N., Carn, S., and Moran, M. D.: A global catalogue of large SO2 sources and emissions derived from the Ozone Monitoring Instrument, Atmos. Chem. Phys., 16, 11497-11519, 10.5194/acp-16-11497-2016, 2016.

Fioletov, V. E., McLinden, C. A., Griffin, D., Abboud, I., Krotkov, N., Leonard, P. J. T., Li, C., Joiner, J., Theys, N., and Carn, S.: Version 2 of the global catalogue of large anthropogenic and volcanic SO2 sources and emissions derived from satellite measurements, Earth Syst. Sci. Data, 15, 75-93, 10.5194/essd-15-75-2023, 2023.

Fioletov, V. E., McLinden, C. A., Krotkov, N., Yang, K., Loyola, D. G., Valks, P., Theys, N., Van Roozendael, M., Nowlan, C. R., Chance, K., Liu, X., Lee, C., and Martin, R. V.: Application of OMI, SCIAMACHY, and GOME-2 satellite SO2 retrievals for detection of large emission sources, J. Geophys. Res. Atmos., 118, 11,399-311,418, https://doi.org/10.1002/jgrd.50826, 2013.

GEM: Tracking the Global Coal Plant Pipeline, Global Energy Monitor, France, 2025.

Hakkarainen, J., Ialongo, I., Koene, E., Szelag, M. E., Tamminen, J., Kuhlmann, G., and Brunner, D.: Analyzing Local Carbon Dioxide and Nitrogen Oxide Emissions From Space Using the Divergence Method: An Application to the Synthetic SMARTCARB Dataset, FRONTIERS IN REMOTE SENSING, 3, 10.3389/frsen.2022.878731, 2022.

Kang, H., Zhu, B., van der A, R. J., Zhu, C., de Leeuw, G., Hou, X., and Gao, J.: Natural and anthropogenic contributions to long-term variations of SO2, NO2, CO, and AOD over East China, AtmRe, 215, 284-293, https://doi.org/10.1016/j.atmosres.2018.09.012, 2019.

Klimont, Z., Smith, S. J., and Cofala, J.: The last decade of global anthropogenic sulfur dioxide: 2000–2011 emissions, Environ. Res. Lett., 8, 014003, 10.1088/1748-9326/8/1/014003, 2013.

Krol, M., van Stratum, B., Anglou, I., and Boersma, K. F.: Estimating NOx emissions of stack plumes using a high-resolution atmospheric chemistry model and satellite-derived NO2 columns, EGUsphere, 2024, 1-32, 10.5194/egusphere-2023-2519, 2024.

Krueger, A., Schaefer, S., Krotkov, N., Bluth, G., and Barker, S.: Ultraviolet Remote Sensing of Volcanic Emissions, GMS, 116, 25-43, 10.1029/GM116p0025, 2000.

Krueger, A. J.: Sighting of El Chichón Sulfur Dioxide Clouds with the Nimbus 7 Total Ozone Mapping Spectrometer, Sci, 220, 1377-1379, doi:10.1126/science.220.4604.1377, 1983.

Kuttippurath, J., Patel, V. K., Pathak, M., and Singh, A.: Improvements in SO2 pollution in India: role of technology and environmental regulations, Environ. Sci. Pollut. Res., 29, 78637-78649, 10.1007/s11356-022-21319-2, 2022.

Levelt, P. F., Oord, G. H. J. v. d., Dobber, M. R., Malkki, A., Huib, V., Johan de, V., Stammes, P., Lundell, J. O. V., and Saari, H.: The ozone monitoring instrument, ITGRS, 44, 1093-1101, 10.1109/TGRS.2006.872333, 2006.

Li, C., McLinden, C., Fioletov, V., Krotkov, N., Carn, S., Joiner, J., Streets, D., He, H., Ren, X., Li, Z., and Dickerson, R. R.: India Is Overtaking China as the World's Largest Emitter of Anthropogenic Sulfur Dioxide, Sci Rep, 7, 14304, 10.1038/s41598-017-14639-8, 2017a.

Li, M., Liu, H., Geng, G. N., Hong, C. P., Liu, F., Song, Y., Tong, D., Zheng, B., Cui, H. Y., Man, H. Y., Zhang, Q., and He, K. B.: Anthropogenic emission inventories in China: a review, Natl. Sci. Rev., 4, 834-866, 10.1093/nsr/nwx150, 2017b.

Liu, M., van der A, R., van Weele, M., Eskes, H., Lu, X., Veefkind, P., de Laat, J., Kong, H., Wang, J., Sun, J., Ding, J., Zhao, Y., and Weng, H.: A New Divergence Method to Quantify Methane Emissions Using Observations of Sentinel-5P TROPOMI, Geophys. Res. Lett., 48, e2021GL094151, https://doi.org/10.1029/2021GL094151, 2021.

Nazari, S., Shahhoseini, O., Sohrabi-Kashani, A., Davari, S., Paydar, R., and Delavar-Moghadam, Z.: Experimental determination and analysis of CO2, SO2 and NOx emission factors in Iran's thermal power plants, Energy, 35, 2992-2998, https://doi.org/10.1016/j.energy.2010.03.035, 2010.

https://doi.org/10.5194/egusphere-2025-4490
Preprint. Discussion started: 24 September 2025


Oppenheimer, C., Scaillet, B., and Martin, R. S.: Sulfur Degassing From Volcanoes: Source Conditions, Surveillance, Plume Chemistry and Earth System Impacts, Reviews in Mineralogy and Geochemistry, 73, 363-421, 10.2138/rmg.2011.73.13, 2011.

Orellano, P., Reynoso, J., and Quaranta, N.: Short-term exposure to sulphur dioxide (SO2) and all-cause and respiratory mortality: A systematic review and meta-analysis, Environ. Int., 150, 106434, https://doi.org/10.1016/j.envint.2021.106434, 2021.

Patel, S.: Thermal Power for Economic Prosperity in India, SSRN Electronic Journal, 2024.

Qu, Z., Henze, D. K., Li, C., Theys, N., Wang, Y., Wang, J., Wang, W., Han, J., Shim, C., Dickerson, R. R., and Ren, X.: SO2 Emission Estimates Using OMI SO2 Retrievals for 2005–2017, J. Geophys. Res. Atmos., 124, 8336-8359, https://doi.org/10.1029/2019JD030243, 2019.

Serbula, S., Ţivkovic, D., Radojevic, A., Kalinovic, T., and Kalinovic, J.: Emission of SO2 and SO42- from copper smelter and its influence on the level of total s in soil and moss in Bor and the surroundings, Hemijska industrija, 69, 18-18, 10.2298/HEMIND131003018S, 2014.

Singh, A. and Agrawal, M.: Acid rain and its ecological consequences, J. Environ. Biol., 29, 15, 2007.

Steinfeld, J. I.: Atmospheric Chemistry and Physics: From Air Pollution to Climate Change, Environment: Science and Policy for Sustainable Development, 40, 26-26, 10.1080/00139157.1999.10544295, 1998.

Taylor, I. A., Preston, J., Carboni, E., Mather, T. A., Grainger, R. G., Theys, N., Hidalgo, S., and Kilbride, B. M.: Exploring the Utility of IASI for Monitoring Volcanic SO2 Emissions, J. Geophys. Res. Atmos., 123, 5588-5606, https://doi.org/10.1002/2017JD027109, 2018.

Theys, N.: TROPOMI Level-2 COBRA SO2 data [data set] [dataset], 2024a.

Theys, N.: TROPOMI Level-2 COBRA SO2 data [data set] [dataset], 2024b.

Theys, N., De Smedt, I., Yu, H., Danckaert, T., van Gent, J., Hörmann, C., Wagner, T., Hedelt, P., Bauer, H., Romahn, F., Pedergnana, M., Loyola, D., and Van Roozendael, M.: Sulfur dioxide retrievals from TROPOMI onboard Sentinel-5 Precursor: algorithm theoretical basis, Atmos. Meas. Tech., 10, 119-153, 10.5194/amt-10-119-2017, 2017.

Theys, N., Fioletov, V., Li, C., De Smedt, I., Lerot, C., McLinden, C., Krotkov, N., Griffin, D., Clarisse, L., Hedelt, P., Loyola, D., Wagner, T., Kumar, V., Innes, A., Ribas, R., Hendrick, F., Vlietinck, J., Brenot, H., and Van Roozendael, M.: A sulfur dioxide Covariance-Based Retrieval Algorithm (COBRA): application to TROPOMI reveals new emission sources, Atmos. Chem. Phys., 21, 16727-16744, 10.5194/acp-21-16727-2021, 2021.

Tomić-Spirić, V., Kovačević, G., Marinković, J., Janković, J., Ćirković, A., Đerić, A. M., Relić, N., and Janković, S.: Sulfur dioxide and exacerbation of allergic respiratory diseases: A time-stratified case-crossover study, J Res Med Sci, 26, 109, 10.4103/jrms.JRMS_6_20, 2021.

Tournigand, P. Y., Cigala, V., Lasota, E., Hammouti, M., Clarisse, L., Brenot, H., Prata, F., Kirchengast, G., Steiner, A. K., and Biondi, R.: A multi-sensor satellite-based archive of the largest SO2 volcanic eruptions since 2006, Earth Syst. Sci. Data, 12, 3139-3159, 10.5194/essd-12-3139-2020, 2020.

Veefkind, J. P., Aben, I., McMullan, K., Förster, H., de Vries, J., Otter, G., Claas, J., Eskes, H. J., de Haan, J. F., Kleipool, Q., van Weele, M., Hasekamp, O., Hoogeveen, R., Landgraf, J., Snel, R., Tol, P., Ingmann, P., Voors, R., Kruizinga, B., Vink, R., Visser, H., and Levelt, P. F.: TROPOMI on the ESA Sentinel-5 Precursor: A GMES mission for global observations of the atmospheric composition for climate, air quality and ozone layer applications, Remote Sens. Environ., 120, 70-83, https://doi.org/10.1016/j.rse.2011.09.027, 2012.

Wang, Y., Wang, J., Xu, X., Henze, D. K., Qu, Z., and Yang, K.: Inverse modeling of SO2 and NOx emissions over China using multisensor satellite data – Part 1: Formulation and sensitivity analysis, Atmos. Chem. Phys., 20, 6631-6650, 10.5194/acp-20-6631-2020, 2020.

World Resources Institute (WRI): Global Power Plant Database [data set] [dataset], 2021.

Yadav, S. and Prakash, R.: Status and Environmental Impact of Emissions from Thermal Power Plants in India, Environmental Forensics, 15, 219-224, 10.1080/15275922.2014.930937, 2014.